JACS Au
AN OPEN ACCESS JOURNAL OF THE AMERICAN CHEMICAL SOCIETY

pubs.acs.org/jacsau
Article

Direct Observation of *In-Focus* Plasmonic Cargos *via* Breaking Angular Degeneracy in Differential Interference Contrast Microscopy

Geun Wan Kim and Ji Won Ha*

Cite This: *JACS Au* 2023, 3, 3436−3445
Read Online

ABSTRACT: Breaking the angular degeneracy arising from the 2-fold optical symmetry of plasmonic anisotropic nanoprobes is critical in biological studies. In this study, we propose differential interference contrast (DIC) microscopy-based focused orientation and position imaging (dFOPI) to break the angular degeneracy of single gold nanorods (AuNRs). Single *in-focus* AuNRs (39 nm × 123 nm) within a spherical mesoporous silica shell were characterized with high throughput and produced distinct doughnut-shaped DIC image patterns featuring two lobes in the peripheral region, attributed to the scattering contribution of the AuNRs with large scattering cross sections. Interestingly, rotation of the lobes was observed in the focal plane for a large AuNR (>100 nm) tilted by more than ∼20° from the horizontal plane as the rotational stage was moved by 10° in a rotational study. From the rotation-dependent characteristic patterns, we directly visualized counterclockwise/clockwise rotations without the angular degeneracy at the localized surface plasmon resonance wavelength. Therefore, our dFOPI method can be applied for *in vivo* studies of important biological systems. To validate this claim, we tracked the three-dimensional rotational behavior of transferrin-modified *in-focus* AuNRs during clathrin-mediated endocytosis in real time without sacrificing the temporal and spatial resolution. In the invagination and scission stage, one or two directed twist motions of the AuNR cargos detached the AuNR-containing vesicles from the cell membrane. Furthermore, the dFOPI method directly visualized and revealed the right-handed twisting action along the dynamin helix in dynamin-catalyzed fission in live cells.

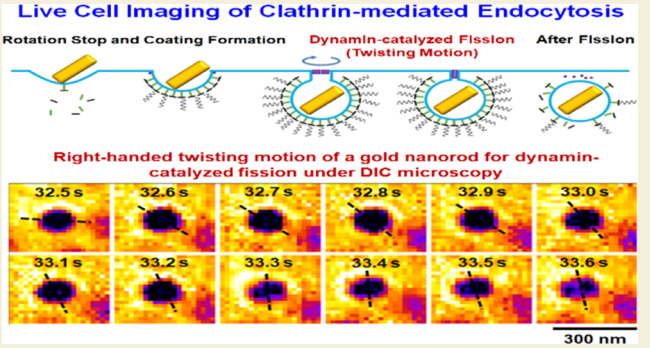

KEYWORDS: *single-particle rotational tracking, gold nanorods, DIC microscopy, angular degeneracy, clathrin-mediated endocytosis, dynamin-assembly twisting*

INTRODUCTION

Local orientation sensing with optical probes is crucial for understanding nanoscale biological processes such as ribozyme folding,[1] myosin walking,[2,3] dynamin-assembly twisting,[4] and ATPase rotation.[3,5,6] Fluorescent molecules are commonly used as the optical sensors in nanoscale orientation sensing.[7−9] However, fluorescent molecules are degraded by stochastic transitions between the off and on states[10,11] and are prone to photobleaching.[12] Recently, anisotropic gold nanorods (AuNRs) have shown promise in overcoming the aforementioned challenges associated with fluorescent probes because their anisotropic shape provides advantageous optical properties[13−15] such as high photostability, large absorption and scattering cross sections,[16] and excellent biocompatibility.[17]

It is essential to overcome the angular degeneracy of a AuNR probe in biological observations. This holds significant importance, as the fundamental biological property lies in the chirality of biomolecules and their assemblies, exemplified by left- or right-handed helices. The focal plane has been utilized to investigate the spatial orientations of individual AuNRs by several polarization-based far-field imaging methods, including dark-field (DF) polarization microscopy,[13] photothermal heterodyne imaging,[18] total internal reflection scattering microscopy,[19] differential interference contrast (DIC) polarization anisotropy,[20−23] and light-sheet microscopy.[24,25] Nevertheless, the significant drawback of polarization-based *in-focus* measurements has been attributed to the angular degeneracy arising from the 2-fold optical symmetry of the AuNR within the four quadrants of the Cartesian coordinate system. In our previous study, we documented a polarization-based *in-focus* method capable of extracting partial three-dimensional (3D) angular information from individual tilted

Received: October 3, 2023
Revised: November 19, 2023
Accepted: November 22, 2023
Published: December 2, 2023

https://doi.org/10.1021/jacsau.3c00594
JACS Au 2023, 3, 3436−3445

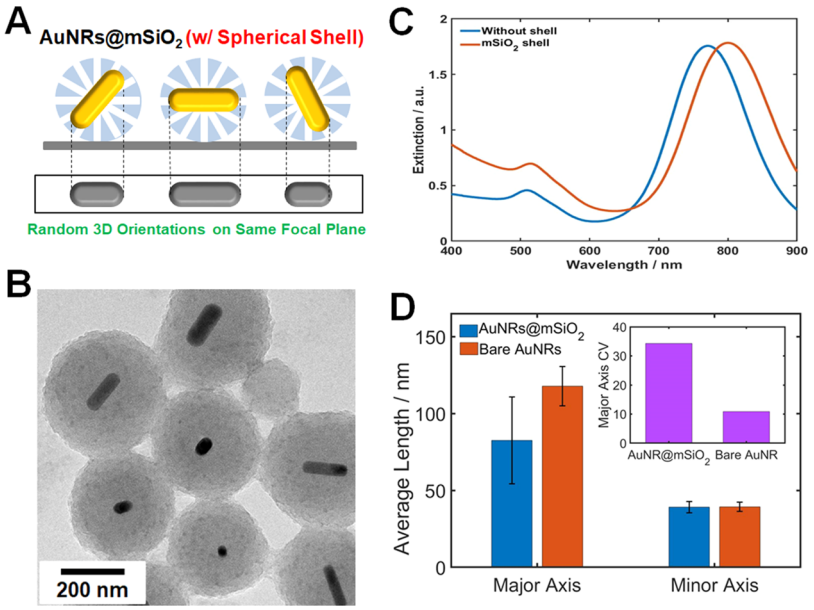

Figure 1. (A) Schematic of the spherical AuNRs@mSiO$_2$ particles with their AuNR cores randomly oriented in the mesoporous silica shell. Their projected lengths depend on their spatial orientations, which are freely available in 3D space. (B) TEM image of the spherical AuNRs@mSiO$_2$. (C) Overlaid UV−vis extinction spectra of the bare AuNRs (blue curve) and spherical AuNRs@mSiO$_2$ (red curve). The anisotropic AuNRs yielded two distinct LSPR peaks. (D) TEM image analysis based on a custom MATLAB script of the length (major axis) and diameter (minor axis) of the AuNRs with and without a spherical mesoporous silica shell. The inset shows the coefficient of variation (CV) values to compare the variation of the major length of both nanoparticles (AuNRs@mSiO$_2$ and bare AuNRs).

AuNRs at the focal plane. This method effectively eliminated the angular degeneracy through integrating DIC polarization anisotropy with DIC image pattern recognition.[22] However, there still exists a need to develop a more accurate and simpler method to overcome the angular degeneracy in DIC polarization anisotropy and directly visualize rotational directions without the need for a cumbersome pattern recognition method.

Recently, the 3D orientations of *out-of-focus* AuNRs have been observed by DF microscopy without angular degeneracy; in particular, by defocused orientation and position imaging (DOPI) techniques,[3,14,26−29] which exploit the electron-transition dipole approximation and the angular anisotropy of dipole radiation. Unfortunately, the low intensity of the DOPI techniques reduces the ability to obtain accurate orientations. To improve the accuracy of orientation angle measurements, DOPI techniques alternate between defocused and focused imaging.[3] Hence, in the realm of biological studies, DOPI techniques face challenges in efficiently tracking fast dynamic motions and orientations with both high spatial and temporal resolution.

To address the difficulties in existing rotational-tracking methods, we propose a DIC microscopy-based focused orientation and position imaging (dFOPI) method. Characterization was conducted on single *in-focus* AuNRs enveloped by a spherical mesoporous silica shell, referred to as AuNRs@mSiO$_2$, at their longitudinal localized surface plasmon resonance (LSPR) wavelength with high throughput under DIC and DF microscopes. We demonstrate the usefulness of the dFOPI method in biological systems by tracking the 3D rotational dynamics of *in-focus* AuNRs without angular degeneracy and with high temporal resolution in live cells. More notably, we directly visualized the action and direction of dynamin-assembly twisting during the invagination and scission stage of clathrin-mediated endocytosis (CME) in live cells.

RESULTS AND DISCUSSION

Synthesis and Characterization of Spherical AuNRs@mSiO$_2$

The current study employed spherical AuNRs@mSiO$_2$ for the following reasons. First, the presence of a spherical outer shell in AuNRs@mSiO$_2$ provides a means to circumvent the LSPR coupling among neighboring AuNRs, offering an advantage for single-particle spectroscopy. Second, when drop-casting is used for sample preparation, AuNRs lacking the shell align parallel to a glass slide, resulting in tilting angles nearly identical to those of the glass slide (see Figure S1). On the contrary, when spherical AuNRs@mSiO$_2$ are placed onto a slide, the AuNRs within the silica shell exhibit random 3D orientations within the identical focal plane (Figure 1A).[30,31] Therefore, high-throughput characterization of image patterns as well as optical properties for individual AuNRs having random 3D orientations within the identical focal plane can be accomplished, overcoming the drawbacks of the conventional gel matrix technique involving the scanning of embedded AuNRs in a vertical direction (Figures S2 and S3).[30,31]

In the present study, we employed large AuNR cores (39 nm × 123 nm, aspect ratio (AR) = 3) covered by a mesoporous spherical silica shell to obtain their 3D orientation-dependent image patterns under DF and DIC microscopy and to better understand the scattering contributions to the final DIC image patterns. The synthesis of spherical AuNRs@mSiO$_2$ followed a protocol from the literature with slight modifications.[32,33] Structural characterization was conducted by scanning electron microscopy (SEM) and transmission electron microscopy (TEM). An SEM image of the synthesized AuNRs before the coating of the mesoporous silica shell is shown in Figure S4,

https://doi.org/10.1021/jacsau.3c00594
JACS Au 2023, 3, 3436−3445

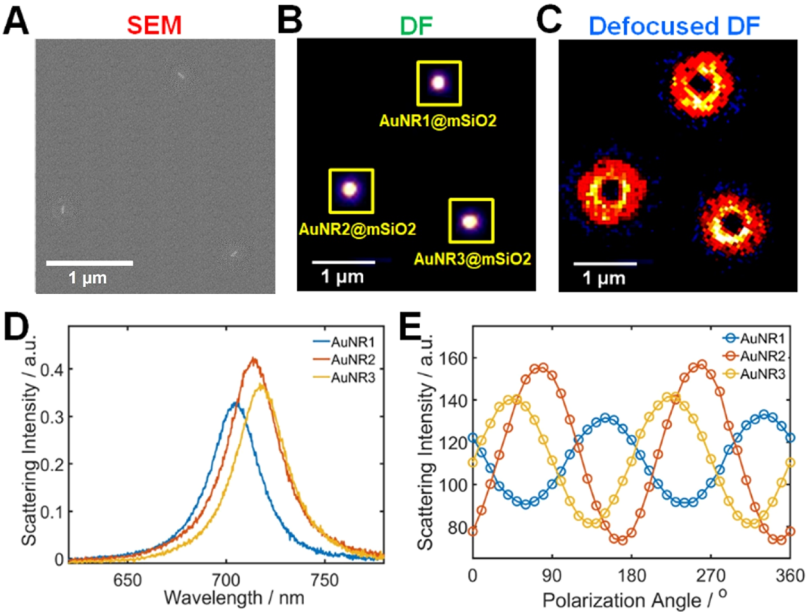

Figure 2. Single-particle correlation study between SEM and DF microscopy. (A) SEM image of three single spherical AuNRs@mSiO$_2$. (B) DF scattering image of the three AuNRs@mSiO$_2$ in (A). (C) Defocused scattering image of the AuNRs@mSiO$_2$. (D) Single-particle scattering spectra of the AuNRs@mSiO$_2$ within the yellow squares indicated in (B). (E) Polarization-dependent scattering intensities of the three AuNRs@mSiO$_2$ as a function of polarization angle from 0 to 360° with 10° steps.

and they have an average diameter and length of 39(±4.2) and 123(±13.7) nm, respectively. Figure 1B illustrates a TEM image of the synthesized AuNRs@mSiO$_2$ after the coating of the spherical silica shell. The approximate thickness of the mesoporous silica shell in a spherical shape was determined to be around 214 (±18.6) nm. Figure 1B demonstrates variations in the projected length of AuNRs within the silica shell, which is influenced by their 3D spatial orientations. Additional SEM and TEM images of many AuNRs are presented in Figures S5 and S6. Figure 1C demonstrates the ensemble spectra of the AuNRs in water. The AuNRs without a silica shell exhibit a longitudinal LSPR peak at 761 nm, whereas the AuNRs@mSiO$_2$ exhibit a longitudinal LSPR peak at 785 nm, indicating a red shift of the peak induced by the presence of the silica shell.

For the statistical analysis of TEM images, numerous AuNRs were measured for each sample, including bare AuNRs and AuNRs@mSiO$_2$. A specialized MATLAB script, incorporating a subroutine within the image processing toolbox of the software, was employed for the analysis of TEM images.[34] As shown in the projected TEM images in Figure 1B,D, the length (major axis) and diameter (minor axis) of the spherical AuNRs@mSiO$_2$ varied much more than those of the AuNRs without a shell. Furthermore, as displayed in the inset of Figure 1D, the coefficient of variation (CV) for AuNRs@mSiO$_2$ surpasses that of bare AuNRs, indicating a higher statistical variation in the major axis of AuNRs@mSiO$_2$. Therefore, electron microscopy techniques confirmed the successful synthesis of AuNRs@mSiO$_2$ with a spherical silica shell. Additionally, the AuNR cores within the shells were observed to have random 3D orientations, as illustrated in Figure 1A.

Single-Particle Correlation Study of Spherical AuNRs@mSiO$_2$

In this single-particle study, we established a correlation among the SEM, DF, and DIC microscopy images of the identical AuNRs (Figures 2 and S7−S8). In this correlation study, identical AuNRs were identified using a TEM grid (Figure S8). The size and shape of the fixed AuNRs on the slide were investigated by using SEM. Through SEM imaging, we guaranteed the measurement of only single AuNRs (Figure 2A). In this study, we first investigated individual AuNRs (39 nm × 123 nm) within a mesoporous silica shell by DF microscopy. The configuration utilized for single-particle microscopy and spectroscopy is presented in Figure S9. An objective lens collected the scattered light by the AuNR cores within the silica shell, directing it to either an EMCCD camera or a spectrograph in DF microscopy (Figure S10).

To ascertain the 3D spatial orientation of individual AuNRs within the silica shell, we utilized the defocused orientation imaging method, relying on the electron-transition dipole approximation.[14] Deliberately shifting the focus away from the nanoprobe's focal plane allows for insights into the orientation of the nanoprobe's emission dipole, achieved through the examination of the scattered field distribution in the blurred image.[14,26] The azimuthal angle (φ) and polar angle (θ) of the AuNRs are defined in Figure S11. Figure 2B displays a correlated DF scattering image of individual AuNRs@mSiO$_2$ on the focal plane, while Figure 2C depicts a defocused image of the scattered light from identical AuNRs@mSiO$_2$, captured with a defocusing distance of approximately 1 μm. Figure 2D shows the scattering spectra for three AuNRs@mSiO$_2$ embedded in water, indicated within the yellow squares in Figure 2B. The average LSPR peak for the three AuNRs@mSiO$_2$ appeared at approximately 714 nm, aligning with the trends seen in the ensemble spectra in Figure 1C. Initially, polarization-dependent imaging was performed under scattering-based DF microscopy for the AuNRs@mSiO$_2$ with linearly polarized light of 700 nm and systematically rotating the polarizer in 10° intervals from 0 to 360°. The scattering intensity of the three AuNRs@mSiO$_2$, as depicted in Figure 2E, exhibited periodic variations with respect to the polarization angle, aligning well with a $\sin^2(\phi)$ function. The 3D

https://doi.org/10.1021/jacsau.3c00594
JACS Au 2023, 3, 3436−3445

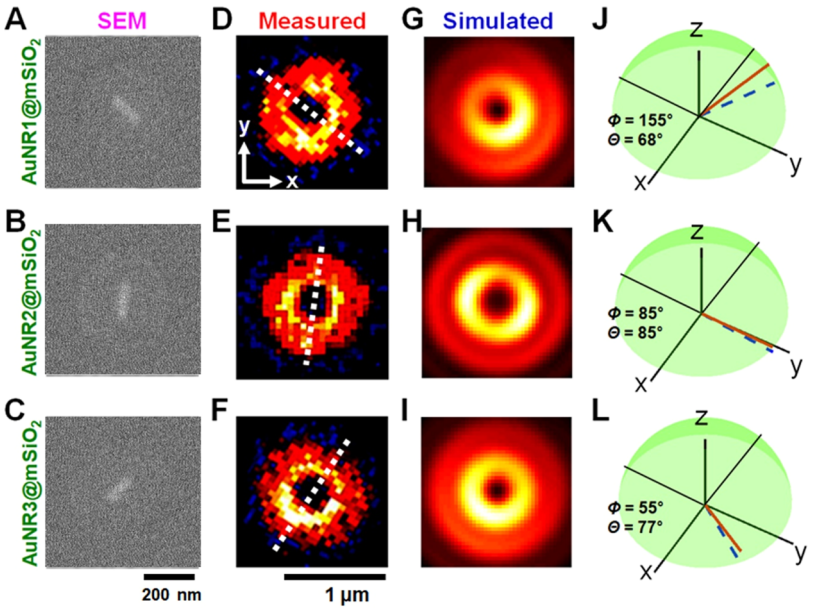

Figure 3. Determination of 3D spatial orientations of the three AuNRs inside the spherical shell through defocused orientation imaging. (A–C) TEM images of spherical (A) AuNR1@mSiO$_2$, (B) AuNR3@mSiO$_2$, and (C) AuNR3@mSiO$_2$. (D–F) Measured defocused image patterns of the three AuNRs@mSiO$_2$. The white dashed line indicates the single dipole orientation. (G–I) Corresponding best-fit simulated scattering patterns for the three AuNRs@mSiO$_2$. (J–L) 3D spatial orientations of the three AuNRs@mSiO$_2$ determined through pattern match analysis. The red line shows the determined 3D orientation and the blue-dotted line is the corresponding in-plane projection.

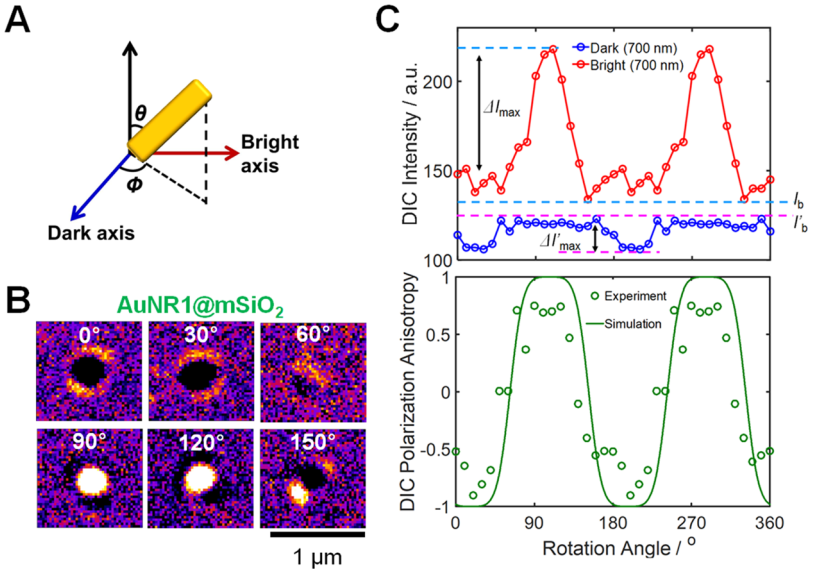

Figure 4. Characterization of spherical AuNRs@mSiO$_2$ under DIC microscopy. (A) Definition of the 2D azimuthal angle φ and the 3D polar angle θ. (B) DIC images of AuNR1@mSiO$_2$ at azimuthal angles φ of 0, 30, 60, 90, 120, and 150° at the LSPR wavelength of 700 nm. A complete set of DIC images at the wavelength is provided in the Supporting Information. (C) DIC intensities (top) and the computed DIC polarization anisotropy P (bottom) of the AuNR at the LSPR wavelength as functions of the rotation angle. I_b and I'_b indicate the bright and dark background intensities, respectively.

spatial orientation of the AuNRs within the shell at the LSPR wavelength had a pronounced effect on the intensities of DF scattering. The distinct in-plane orientations within the spherical shell are supported by the observed phase difference among the three AuNRs@mSiO$_2$.

Detailed analysis was carried out on the defocused images (Figure 2C) for determining the polar angle (θ) and azimuthal angle (φ) of the three AuNRs@mSiO$_2$. AuNRs, significantly smaller than the incident light wavelength, can be treated as electric point dipoles.[14] In accordance with the electrostatic approximation, we can quantify the collective scattering electric field emanating from an AuNR by linearly superimposing three distinct scattering electric fields (Figure S11).[14,35] Consequently, we can resolve the spatial orientation of a single AuNR through analyzing the field distribution from each dipole.

As illustrated in Figure 2B, the scattered light by a AuNR was concentrated into a solid bright spot at the focal plane, offering limited insight into the 3D spatial orientation of the AuNR emission dipole. Nevertheless, when the AuNR was

https://doi.org/10.1021/jacsau.3c00594
JACS Au 2023, 3, 3436–3445

situated approximately 1 μm away from the focal plane, the distribution of the scattering intensity in the blurred image yielded information regarding the orientation of the AuNR emission dipole (Figures 2C and 3). The in-plane orientation angle φ can be easily derived from the two-lobe scattering pattern that demonstrates an angular anisotropy (Figure 3D–F). In this study, the program developed by Enderlein and Böhmer was utilized for estimating the polar angle θ. The program calculates the distinctive intensity distribution originating from an emitter having three emission dipoles oriented perpendicularly, each possessing different emission strengths.[36,37] We can estimate the spatial orientation of AuNRs by referring to their corresponding field map. The most accurate calculated scattering patterns were achieved through fine-tuning the parameters that define the orientation angles and emission strength from three orthogonal dipoles in the AuNRs (Figure 3G–I). Toprak et al. conducted measurements on the 3D orientation and stepping behavior of individual bifunctional rhodamine probes linked to one of the calmodulins in the light-chain domain (LCD) of myosin V while it traverses along actin. The reported angular accuracy of DOPI of the fluorescent molecules was approximately ±5°.[3] In this investigation, the azimuthal and polar angles of AuNR1@mSiO$_2$ were ascertained as 68 and 155°, respectively, by comparing the measured scattering pattern with the simulated scattering pattern that provided the best fit (Figure 3J).[14,38] Furthermore, the azimuthal and polar angles of AuNR2@mSiO$_2$ and AuNR3@mSiO$_2$ were approximated to be 85 and 85° (Figure 3K), and 55 and 77° (Figure 3L), respectively. Thus, through the application of defocused imaging, we were able to efficiently characterize the 3D spatial orientations of individual AuNR cores (39 nm × 123 nm) enveloped in a shell within a single frame on the identical focal plane. These findings were in agreement with the 2D orientations identified through SEM imaging (Figure 3A–C).

Next, we examined the three fixed AuNRs@mSiO$_2$ (Figure 2) under DIC microscopy, specifically at 700 nm near their LSPR wavelength (Figure S12). High-throughput DIC orientation imaging of individual AuNRs within the spherical shell in the same focal plane was achieved (Figure S13),[30,31] and DIC signals from the AuNRs within the silica shell were used for investigating their characteristic optical properties.[30,31] To explore the dependence on wavelength and polarization, a rotational analysis of AuNR1@mSiO$_2$ was conducted by incrementally rotating a stage in 10° steps from 0 to 360° at the LSPR wavelength. Figure 4A illustrates the definition of the polar angle θ and azimuthal angle φ of the AuNR in DIC microscopy. The DIC images of AuNR1@mSiO$_2$ at 700 nm exhibited periodic variations corresponding to the rotation angle (Figures 4B and S14). Moreover, the brightness and darkness of AuNR1@mSiO$_2$ exhibited periodic variations that were observed to be anticorrelated at the LSPR wavelength. This indicates that an increase in bright intensity corresponds to a decrease in dark intensity and vice versa (Figure 4C). The bright and dark intensities were well represented by $\sin^4(\varphi)$ and $\cos^4(\varphi)$ functions at each LSPR wavelength, respectively. Thus, the bright and dark intensities of the AuNR can be formulated as[12,18]

$$I_B \propto \sin^4(\varphi)\sin^2(\theta)$$
$$I_D \propto \cos^4(\varphi)\sin^2(\theta) \quad (1)$$

respectively. We can directly compute the spatial AuNR orientation using the bright and dark intensities, as given in eq 1. However, in practical scenarios, precision might be influenced by vertical focus drifting, intensity fluctuations in the light source, and other factors. To mitigate these effects, we instead calculate the DIC polarization anisotropy P as[20,21]

$$P = \frac{I_{B,N} - I_{D,N}}{I_{B,N} + I_{D,N}} \quad (2)$$

where $I_{B,N}$ and $I_{D,N}$ are the normalized bright and dark intensities at the LSPR wavelength, respectively. The DIC polarization anisotropy of AuNR1@mSiO$_2$ ranged from −1 (when the AuNR aligned with the dark axis, φ = 0° or 180°) to 1 (when the AuNR aligned to the bright axis, φ = 90° or 270°) (Figures 4C and S15). Expressed as intensity ratios, the DIC polarization anisotropy experiences fewer impacts from fluctuations in intensity when compared to the absolute-intensity form, making it a more accurate and reliable method for angle measurements.[21] Furthermore, the DIC polarization anisotropy is determined exclusively by the azimuthal angle φ and does not necessitate consideration of the polar angle θ of the AuNR.[20]

Breaking the Angular Degeneracy of *In-Focus* AuNR in DIC Microscopy

Comprehending the direction of rotation is crucial for deciphering the fundamental mechanisms of biological processes that encompass chiral biomolecules and their assemblies, such as left- or right-handed helices. Thus, far, the 3D orientations of *out-of-focus* AuNRs have been resolved by defocused orientation imaging methods, which remove the angular degeneracy but greatly reduce the intensity. In myosin analysis, Toprak et al. reported that owing to the low intensity in the defocused imaging mode, the temporal resolution of DOPI is only 1–2 fps.[3] Thus, defocused imaging methods are better suited for characterizing static events than dynamic events.

Besides the DOPI techniques, angular degeneracy (Figure S16) has been recognized as a significant limitation of polarization-based *in-focus* measurements. As the azimuthal angles $+\varphi$ and $-\varphi$ in the four quadrants cannot be resolved, ambiguous rotational motions such as counterclockwise/clockwise rotations cannot be distinguished. However, in the previous study, we presented that through the combination of DIC image pattern recognition with DIC polarization anisotropy, it becomes possible to overcome the limitation of angular degeneracy in single *in-focus* AuNRs (25 nm × 73 nm, AR = 3) tilted relative to the horizontal plane.[22] It is worth noting that four different image patterns were used for identifying the precise quadrant where the AuNR was located. However, continued efforts need to be made to develop more efficient and accurate polarization-based methods to go beyond the previous pattern recognition method allowing for the identification of the exact quadrant only, and to directly visualize detailed rotational directions of single *in-focus* AuNRs with high angular resolution.

In this paper, we proposed the dFOPI technique to break the angular degeneracy in DIC polarization anisotropy by directly visualizing rotational directions and to overcome the limitations of current DOPI techniques. As shown in Figure S17, we found that some AuNR cores showed distinct doughnut DIC patterns having two lobes in the peripheral area in the same focal plane, as indicated by a black arrow. The

https://doi.org/10.1021/jacsau.3c00594
JACS Au 2023, 3, 3436–3445

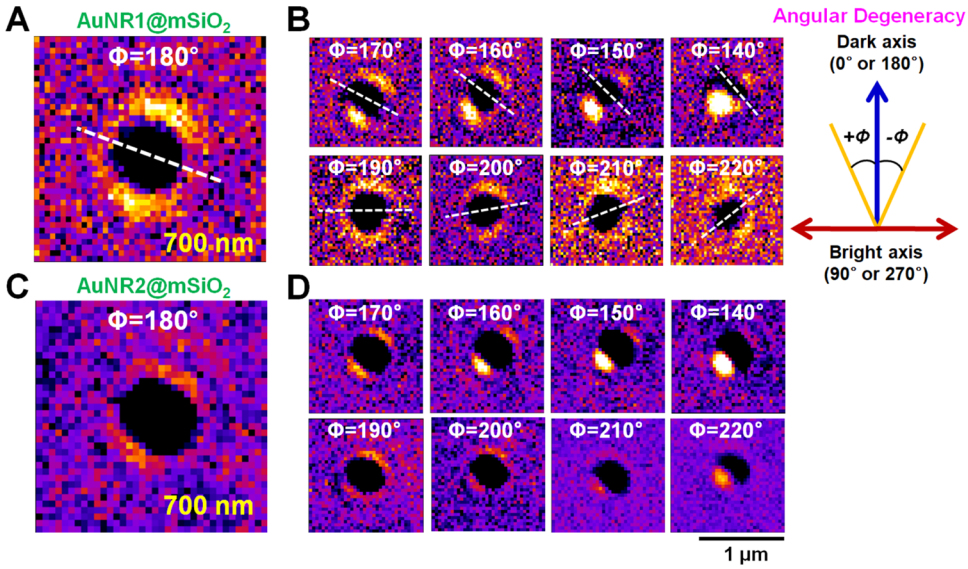

Figure 5. Breaking the angular degeneracy in DIC microscopy. (A) Doughnut-shaped image pattern of AuNR1@mSiO$_2$ measured at 700 nm. The azimuthal angle is 180°. (B) DIC image patterns of an Anura as the azimuthal angle φ varies from 140 to 220° in 10° increments. The white dotted lines indicate the orientation of the AuNR. The azimuthal angle is easily distinguished as + φ or −φ with respect to the dark axis. (C) Doughnut-shaped image pattern of AuNR2@mSiO$_2$ at 700 nm. (D) DIC image patterns of the AuNR as φ varies from 140 to 220° in 10° steps.

resultant image in DIC microscopy is formed through the interference of two mutually shifted, phase-delayed, and orientation-sensitive scattering images (Figure S12). Consequently, the distribution of the electromagnetic field can be encoded artificially into the DIC point spread function (PSF), creating distinguishable DIC image patterns of *in-focus* AuNRs with different orientations.[22] The scattering cross sections of plasmonic nanoparticles are typically 4−5 orders of magnitude greater than those of fluorescent dye molecules,[11,13] therefore, the relatively strong scattered light from the AuNR (>100 nm; Figure 1B) in 3D space can be projected onto the DIC PSF. In this way, the scattered light significantly contributes to the final DIC image patterns (Figure S12), as also supported by our previous work.[22] For further confirmation, we imaged single AuNRs (25 nm × 73 nm, Figure S18) with the same AR of 3 by DIC microscopy while rotating the stage in steps of 10° at the LSPR wavelength (700 nm) of the AuNRs. When the AuNRs were drop-cast, they lay flat on the glass slide, and the two lobes in their peripheral area were barely visible (Figure S19). However, the two lobes of larger AuNRs with the same AR (39 nm × 123 nm) were highly visible at 700 nm (Figures 5 and S14). Furthermore, the two lobes contrasted most strongly when an AuNR was aligned along the dark polarization direction (φ = 0 or 180°), and the contrast reduced as the AuNR rotated away from the axis (Figures 5 and S14). It should be noted that a completely dark DIC pattern was observed in principle for a single AuNR when it was aligned with the dark polarization direction (Figure 4A, φ = 0 or 180°) under DIC microscopy. Therefore, the rotation-dependent contrast in Figure 5 can be attributed to the polarization-sensitive scattering intensity arising when the AuNRs were excited by the two linearly polarized beams of the DIC microscope and the appearance of the lobes in large AuNRs (>100 nm) is attributed to the scattering contribution to their DIC image patterns.

More notably, the lobes of AuNR1@mSiO$_2$ with a polar angle of 68° (or a tilting angle of 22° from the horizontal plane) rotated as the rotational stage was moved by 10° in the focal plane (Figure 5B). The complete set of DIC images of AuNR1@mSiO$_2$ at 700 nm were collected and are shown in Figure S20. The rotation of the two lobes depended on the angle of rotation. Thus, the spatial 2D orientation of a AuNR was directly estimable from the DIC image patterns, and the azimuthal angles −φ and +φ can be distinguished with respect to the polarization direction in the focal plane. Moreover, the doughnut-shaped DIC patterns with two lobes were also observed for AuNR2@mSiO$_2$ and AuNR3@mSiO$_2$ with polar angles of 85 and 77°, respectively, but were not rotated with the rotational angle (Figures 5D and S21−S22). This suggests that in the final DIC PSF of the AuNR (Figure 5), the lobe rotations were associated with tilting of the AuNR from the horizontal plane. From the repeated measurements with more AuNRs@mSiO$_2$, we deduced that the cutoff θ to show the lobe rotations was about 70°. This result is consistent with the cutoff θ of 70° to show a sufficient difference between the DIC images of a tilted AuNR and a flat-lying AuNR (25 nm × 73 nm) in our previous study.[22] Furthermore, the rotations of the lobes with distinct image patterns can be ascribed to the scattered light from the inclined AuNR, which was projected onto slightly varied positions in the interfered DIC images, as also supported by our previous work.[22] In addition to the static study, the rotations of the two lobes were further captured in a video recording of the bare AuNR1 (39 nm × 123 nm, without the shell) rotating on a synthetic membrane with the lobe rotations (Figure S23 and Movie S1), indicating that the dynamics can be observed on frame-rate time scales.

Twisting Motions and Directions of Single AuNRs during CME

Gaining insight into the translational and rotational movements of single AuNRs on cell membranes has the potential for enhancing our comprehension of essential cellular processes such as drug delivery mechanisms and endocytosis. Thus, as a next step, we chose transferrin-modified AuNRs (39 nm × 123 nm, without the shell) undergoing rotation on cell membranes as a representative model system. This aimed to confirm the usefulness and applicability of this technique in tracking and

https://doi.org/10.1021/jacsau.3c00594
JACS Au 2023, 3, 3436−3445

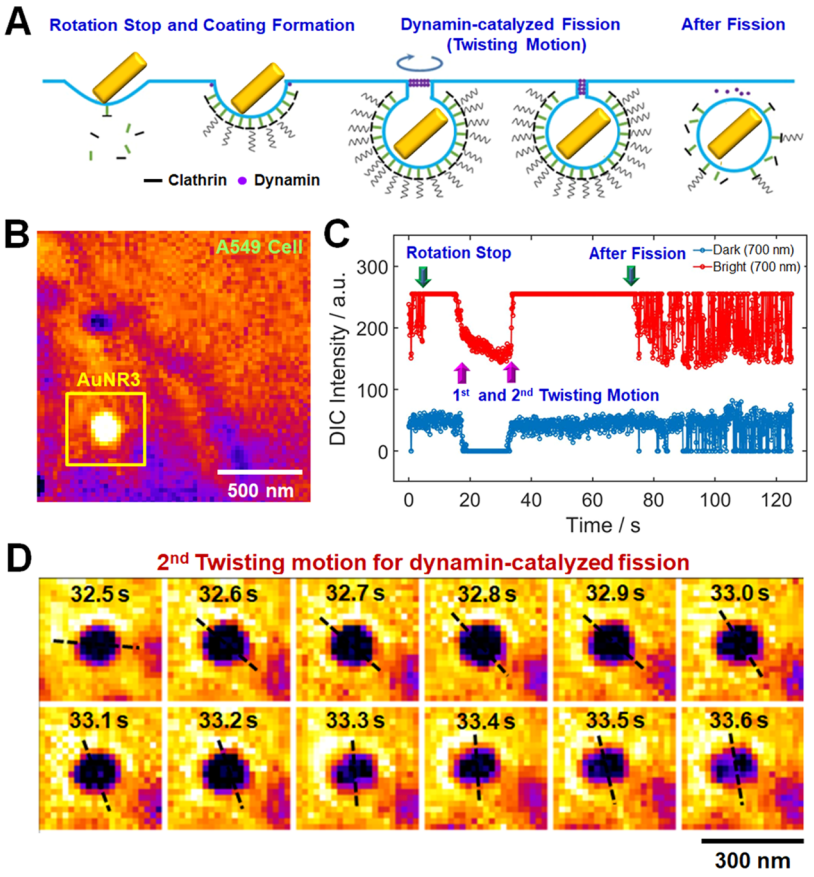

Figure 6. DIC imaging of a transferrin-coated AuNR without the shell during clathrin-mediated endocytosis (CME). (A) Schematic of the complete CME process, which internalizes the AuNR in the A549 cell. (B) DIC image of AuNR3 landed on the cell membrane. (C) Changing DIC intensities of AuNR3 in the two polarization directions during the CME process. (D) Tracking the direction of AuNR3 during the second twisting action through the changing DIC pattern. The characteristic doughnut-shaped patterns of AuNR3 with two lobes rotate to the right over time.

resolving rapid rotational dynamics in real biological systems such as receptor-mediated endocytosis (or CME). In this study, transferrin-coated AuNRs, lacking the silica shell, were employed to induce their selective attachment to transferrin receptors on the cell membrane, facilitating CME. In addition, transferrin-coated AuNRs without the shell will give the same result as AuNRs having the silica shell (AuNRs@mSiO$_2$) under DIC microscopy. Being based on interferometry principles, DIC microscopy is ideally suited to decipher the rotational dynamics of AuNRs in live cell imaging.[20,22] DIC microscopy resolves the difference in the optical path between two polarized beams (B1 and B2) that are separated by a Nomarski prism and oriented perpendicular to each other (Figure S12). This interference-based method is immune to the influence of light scattered by neighboring cellular components and retains a high-throughput capacity. Therefore, it is advantageous for single-particle rotational tracking and can study fast rotations in live cells.

In this study, we captured a video (Movie S2) with a temporal resolution of 100 ms (10 fps) at 700 nm, illustrating the rotational motions of bare AuNR2 on a live cell membrane (Figure S24A). 10-consecutive frames were selected from Movie S2 that displays clear DIC image patterns and transitions of two lobes (Figure S24B). Notably, the azimuthal angle φ and the rotational directions of *in-focus* AuNR2 were directly visualized and tracked from the focused DIC patterns with two lobes (Movie S2). DIC polarization anisotropy was calculated based on 10 images to ascertain the azimuthal angle φ, while DIC image patterns were utilized to observe rotational directions within the four quadrants (Figure S24C), followed by the determination of polar angle θ by eq 1 (Figure S24D). More detailed procedures for determining 3D orientation angles are provided in the Supporting Information (2−9 and 2−10). Therefore, we demonstrated that the dFOPI method can be effectively used for tracking the 3D orientations and rotational directions of single AuNR probes in the focal plane without angular degeneracy and scalifying the reduced signal intensity and temporal resolution in dynamic biological environments.

Beyond the demonstration in biological systems, we further used the dFOPI technique to answer real biological questions in *in vivo* biological systems. We tracked and revealed the endocytosis process in live cells by employing transferrin-modified AuNRs as a model system. Endocytosis is a fundamental cellular process that transports substances into the cell. Among the various endocytic pathways, CME is a vital process through which cells internalize various biological components by enveloping them within the cell membrane.[39] Dynamins participate in the ultimate scission stage of CME, leading to the release of newly formed vesicles.[4,40−43] Different models, such as twisting[4,43] and constriction,[44−46] have been proposed to elucidate how dynamin assembly severs the neck of the clathrin-coated pit (CCP). According to the constriction and twisting models,[4] dynamin molecules self-assemble into a helical collar structure at the neck of the nascent vesicle, and the helical dynamin assembly generates a twisting motion

https://doi.org/10.1021/jacsau.3c00594
JACS Au 2023, 3, 3436−3445

during guanosine-5′-triphosphate (GTP) hydrolysis.[4] The twisting motion produces a longitudinal tension that breaks the vesicle from the cell membrane.

In this study, we recorded a movie (Movie S3, 10 fps) that characterizes the rotational motions and internalization of a tilted AuNR during the CME process of A549 cells. By removing the angular degeneracy, our proposed dFOPI technique allowed for visualization of the twisting motions and directions (right-handed or left-handed) of the dynamin assembly during the CME process, which has been a challenge previously in revealing the CME mechanism (*e.g.*, twisting direction) in live cells. Figure 6A schematizes the complete CME process that internalized transferrin-coated AuNR3 (without the shell) in A549 cells. Initially, transferrin-coated AuNR appeared on the cell membrane, indicating cellular uptake of the AuNR (Figure 6B). The fast rotation of AuNR3 on the membrane manifested in flickering images and fluctuating DIC intensities (Figure 6C). The flickering images were convenient representations of the rotating AuNR3 on the cell membrane. Over time, the rotational freedom of the AuNR on the A549 cell membrane diminished gradually. The slowed rotational motions yielded increasingly fewer fluctuations in the DIC intensities (Figure 6A,C). The gradual loss of rotational freedom indicated that the AuNR was enclosed in CCPs. At 1.7 s, the rotational motions of the AuNR ceased for several tens of seconds.[43,47] When the rotation completely ceased (at 4.80−15.2 s), the AuNR intensity remained bright and nearly constant. Thereafter, the AuNR intensity in the DIC image changed from completely bright to dark, indicating that the AuNR3 rotated by ∼90° (the first twisting motion in Figure 6C). The dark intensity remained nearly constant from 19.2 to 33.1 s, then reverted to completely bright, indicating the second twisting motion through 90° (Figure 6C). The second bright image remained at 74.1 s. At this time, the DIC image of the AuNR transitioned from bright to dark, followed by intermittent flickering images, indicating that the active rotational motion was regained after the fission (Figure 6C). Finally, the internalized vesicle was translated from the original entry spot. During the CME process, the 2D *in-plane* orientation of the AuNR3, shown in Figure 6C, was determined from the DIC polarization anisotropy P (Figure S25, Supporting Information 2−11). Afterward, the 3D *out-of-plane* orientation of the AuNR3 can be determined by eq 1, as clearly demonstrated in Figure S24D.

The important observations in Figure 6 require further discussion. First, the AuNR3 was twisted once or twice before scission of the CCPs (Figure 6C), consistent with the previous studies.[43,47] We, therefore, confirmed that dynamin provides the dominant driving force that removes buds from the cell membrane by twisting motions.[40] Second, dynamin is a right-handed helix, and reportedly demonstrates right-handed twisting activity (or corkscrew-like motions) along the dynamin helix, which tightens and constricts it for catalyzing the fission process.[48,49] To reveal the right-handed twisting activity, which has been experimentally detected using defocused DF imaging with much reduced intensity, X-ray crystallography, and cryo-electron microscopy,[43,48,49] we carefully tracked the twisting direction of AuNR3 during the second twisting action, observing a shift in the DIC pattern from entirely dark to entirely bright (Movie S3). Figure 6D shows the characteristic doughnut-shaped patterns of AuNR3 with two lobes. More interestingly, both lobes rotated to the right over time (indicated by the black dotted line of Figure 6D). The complete set of DIC images during the second twisting motion is presented in Figure S26. Therefore, by combining our dFOPI technique with *in-focus* AuNR probes, we could directly visualize and elucidate the right-handed twisting motions of dynamin-catalyzed membrane fission during the *in vivo* CME process.

CONCLUSIONS

In summary, we presented a dFOPI method to break the angular degeneracy of single AuNRs by directly visualizing rotational directions and to overcome the limitations of current DOPI techniques. Single *in-focus* AuNRs (39 nm × 123 nm) inside a mesoporous spherical silica shell generated distinctive doughnut-shaped DIC image patterns, featuring two lobes in the peripheral area owing to the scattering contribution of the AuNRs. More interestingly, a rotation of the lobes was observed on the focal plane for the AuNRs tilted by more than ∼20° from the horizontal plane as the rotational stage was moved by 10° in a 360° rotational study. Therefore, our proposed dFOPI technique allowed us to directly observe counterclockwise or clockwise rotations without angular degeneracy and to resolve the 3D orientations for single *in-focus* AuNRs without sacrificing temporal and spatial resolution. The dFOPI technique effectively tracked the 3D orientations of the AuNRs as they rotated on A549 cell membranes, validating the usefulness and applicability of the technique in *in vivo* biological systems. More importantly, we tracked the characteristic rotational motions of an *in-focus* AuNR during the CME process in a live cell. We observed the dynamin-induced twisting activity that tenses the neck of the endocytic vesicle prior to scission. Our dFOPI technique revealed a right-handed twisting motion of the *in-focus* tilted AuNR during the dynamin-catalyzed fission of live cells.

EXPERIMENTAL METHODS

Characterization of AuNRs@mSiO$_2$

Both transmission electron microscopy (TEM, JEL-2100F, JEOL, Japan) and scanning electron microscopy (SEM, JSM-6500, JEOL, Japan) were utilized for structural analyses of AuNRs@mSiO$_2$. Moreover, a UV−vis spectrometer from Agilent Technologies was utilized for recording heterogeneous LSPR ensemble spectra for bare AuNRs and AuNRs@mSiO$_2$ in water.

Sample Preparations for Single-Particle Microscopy and Spectroscopy

The procedure for preparing samples for single-particle investigations is outlined as follows. Initially, the colloidal solution of AuNRs@mSiO$_2$ was thinned with distilled water. Afterward, the thinned solution underwent sonication at room temperature for 10 min. Subsequently, we prepared samples through applying the thinned solution onto precleaned glass slides using drop-casting. The prepared slide was then covered with a 22 mm × 22 mm No. 1.5 coverslip from Corning, NY. In entire experimental procedures, the density of AuNRs@mSiO$_2$ casted onto the slide was consistently kept at around 1.0 μm^{-2} to enable the characterization of individual AuNRs.

DF Microscopy and Spectroscopy

DF imaging was carried out using an in-house setup consisting of a Nikon inverted microscope (ECLIPSE Ti−U, Japan), an EMCCD camera (iXon Ultra 897, U.K.), and specialized image analysis software. In DF mode, a Nikon DF condenser and a Nikon Plan Fluor 100 × 0.5−1.3 oil iris objective lens were employed. DF scattering images of AuNRs within a silica shell were captured by an Andor iXonEM+ CCD camera. The acquired images underwent analysis with ImageJ software. Additionally, DF spectra were obtained by using an Andor CCD camera (Newton DU920P-OE, U.K.) and an

https://doi.org/10.1021/jacsau.3c00594
JACS Au 2023, 3, 3436−3445

Andor spectrometer (SHAMROCK 303i, SR-303I-A, U.K.). In the analysis process, the scanning stage was manipulated to position the sample at the designated location, ensuring that the objective lens collected the scattered light only from the chosen area. The scattered light was subsequently guided to the spectrometer, where it underwent dispersion by a grating (300 lines/mm) and was captured by a Newton CCD camera (Andor, U.K.). The background spectrum was obtained from a particle-free region.

DIC Microscopy

A Nikon inverted microscope (ECLIPSE Ti−U, JAPAN) equipped with two polarizers, a pair of Nomarski prisms, and a quarter-wave plate was used for DIC microscopy. The prepared samples were irradiated with an oil-immersion condenser featuring a numerical aperture (NA) of 1.4. An objective lens (Plan Apo oil-immersion type, 100×, NA = 1.4) was used for gathering the DIC signals emanating from the sample. High-quality DIC images were captured using an Andor EMCCD camera (iXon Ultra 897, U.K.) and subsequently analyzed with ImageJ and MATLAB.

■ ASSOCIATED CONTENT

Supporting Information

The Supporting Information is available free of charge at https://pubs.acs.org/doi/10.1021/jacsau.3c00594.

Materials and chemicals; preparation of AuNRs encapsulated with silica shell; cell culture; rotational study under DIC microscopy; determining the azimuthal angle of AuNR in DIC microscopy; DIC polarization anisotropy; defocused orientation imaging, simulation of scattering patterns of AuNRs; preparation of synthetic membrane on glass slide; scattering contribution to DIC image of single AuNR, *etc*; single particle correlation study between DF microscopy and DIC microscopy; photograph to show the experimental setup for single particle microscopy and spectroscopy, and working principle of DIC microscopy (PDF)

Movie to show the characteristic doughnut-shaped DIC image patterns of in-focus AuNR while rotating on the synthetic membrane, this movie was recorded at the temporal resolution of 100 ms (10 frames per second, fps) (Movie S1) (AVI)

Movie to show the characteristic doughnut-shaped DIC image patterns of in-focus AuNR while rotating on the live cell membrane, this movie was recorded at the temporal resolution of 100 ms (10 fps) (Movie S2) (AVI)

Movie to show the characteristic DIC image patterns of in-focus AuNR3 during the clathrin-mediated endocytosis process in live cell, this movie was recorded at the temporal resolution of 100 ms (10 fps) (Movie S3) (AVI)

■ AUTHOR INFORMATION

Corresponding Author

Ji Won Ha − *Department of Chemistry, University of Ulsan, Ulsan 44610, South Korea; Energy Harvest-Storage Research Center (EHSRC), University of Ulsan, Ulsan 44610, South Korea;* orcid.org/0000-0003-0566-8176; Phone: +82-52-712-8012; Email: jwha77@ulsan.ac.kr; Fax: +82-52-712-8002

Author

Geun Wan Kim − *Department of Chemistry, University of Ulsan, Ulsan 44610, South Korea*

Complete contact information is available at: https://pubs.acs.org/10.1021/jacsau.3c00594

Notes

The authors declare no competing financial interest.

■ ACKNOWLEDGMENTS

This work was supported by two National Research Foundation of Korea (NRF) grants funded by the Korean government (MSIP) (Nos. RS-2023-00208346 and 2019R1A6A1A11053838).

■ REFERENCES

(1) Denesyuk, N. A.; Thirumalai, D. How do metal ions direct ribozyme folding? *Nat. Chem.* **2015**, *7* (10), 793−801.

(2) Molloy, J. E.; Veigel, C. Myosin motors walk the walk. *Science* **2003**, *300* (5628), 2045−2046.

(3) Toprak, E.; Enderlein, J.; Syed, S.; McKinney, S. A.; Petschek, R. G.; Ha, T.; Goldman, Y. E.; Selvin, P. R. Defocused orientation and position imaging (DOPI) of myosin V. *Proc. Natl. Acad. Sci. U.S.A.* **2006**, *103* (17), 6495−6499.

(4) Roux, A.; Uyhazi, K.; Frost, A.; De Camilli, P. GTP-dependent twisting of dynamin implicates constriction and tension in membrane fission. *Nature* **2006**, *441* (7092), 528−531.

(5) Zhuang, X.; Bartley, L. E.; Babcock, H. P.; Russell, R.; Ha, T.; Herschlag, D.; Chu, S. A Single-molecule study of RNA catalysis and folding. *Science* **2000**, *288* (5473), 2048−2051.

(6) Nishizaka, T.; Oiwa, K.; Noji, H.; Kimura, S.; Muneyuki, E.; Yoshida, M.; Kinosita, K. Chemomechanical coupling in F1-ATPase revealed by simultaneous observation of nucleotide kinetics and rotation. *Nat. Struct. Mol. Biol.* **2004**, *11*, 142−148.

(7) Khatua, S.; Guerrero, J. M.; Claytor, K.; Vives, G.; Kolomeisky, A. B.; Tour, J. M.; Link, S. Micrometer-scale translation and monitoring of individual nanocars on glass. *ACS Nano* **2009**, *3* (2), 351−356.

(8) Forkey, J. N.; Quinlan, M. E.; Goldman, Y. E. Protein structural dynamics by single-molecule fluorescence polarization. *Prog. Biophys. Mol. Biol.* **2000**, *74* (1−2), 1−35.

(9) Chung, I.; Shimizu, K. T.; Bawendi, M. G. Room temperature measurements of the 3D orientation of single CdSe quantum dots using polarization microscopy. *Proc. Natl. Acad. Sci. U.S.A.* **2003**, *100* (2), 405−408.

(10) Moerner, W. E.; Orrit, M. Illuminating single molecules in condensed matter. *Science* **1999**, *283* (5408), 1670−1676.

(11) Nirmal, M.; Dabbousi, B. O.; Bawendi, M. G.; Macklin, J. J.; Trautman, J. K.; Harris, T. D.; Brus, L. E. Fluorescence intermittency in single cadmium selenide nanocrystals. *Nature* **1996**, *383*, 802−804.

(12) Xie, X. S.; Dunn, R. C. Probing single molecule dynamics. *Science* **1994**, *265* (5170), 361−364.

(13) Sönnichsen, C.; Alivisatos, A. P. Gold nanorods as novel nonbleaching plasmon-based orientation sensors for polarized single-particle microscopy. *Nano Lett.* **2005**, *5* (2), 301−304.

(14) Xiao, L.; Qiao, Y.; He, Y.; Yeung, E. S. Three dimensional orientational imaging of nanoparticles with darkfield microscopy. *Anal. Chem.* **2010**, *82* (12), 5268−5274.

(15) Wang, G.; Sun, W.; Luo, Y.; Fang, N. Resolving rotational motions of nano-objects in engineered environments and live cells with gold nanorods and differential interference contrast microscopy. *J. Am. Chem. Soc.* **2010**, *132* (46), 16417−16422.

(16) Jain, P. K.; Lee, K. S.; El-Sayed, I. H.; El-Sayed, M. A. Calculated absorption and scattering properties of gold nanoparticles of different size, shape, and composition: applications in biological imaging and biomedicine. *J. Phys. Chem. B* **2006**, *110* (14), 7238−7248.

(17) Murphy, C. J.; Gole, A. M.; Stone, J. W.; Sisco, P. N.; Alkilany, A. M.; Goldsmith, E. C.; Baxter, S. C. Gold nanoparticles in biology:

beyond toxicity to cellular imaging. *Acc. Chem. Res.* **2008**, *41* (12), 1721−1730.
(18) Chang, W.-S.; Ha, J. W.; Slaughter, L. S.; Link, S. Plasmonic nanorod absorbers as orientation sensors. *Proc. Natl. Acad. Sci. U.S.A.* **2010**, *107* (7), 2781−2786.
(19) Marchuk, K.; Ha, J. W.; Fang, N. Three-dimensional high-resolution rotational tracking with superlocalization reveals conformations of surface-bound anisotropic nanoparticles. *Nano Lett.* **2013**, *13* (3), 1245−1250.
(20) Ha, J. W.; Sun, W.; Stender, A. S.; Fang, N. Dual-wavelength detection of rotational diffusion of single anisotropic nanocarriers on live cell membranes. *J. Phys. Chem. C* **2012**, *116* (4), 2766−2771.
(21) Ha, J. W.; Sun, W.; Wang, G.; Fang, N. Differential interference contrast polarization anisotropy for tracking rotational dynamics of gold nanorods. *Chem. Commun.* **2011**, *47* (27), 7743−7745.
(22) Xiao, L.; Ha, J. W.; Wei, L.; Wang, G.; Fang, N. Determining the full three-dimensional orientation of single anisotropic nanoparticles by differential interference contrast microscopy. *Angew. Chem., Int. Ed.* **2012**, *51* (31), 7734−7738.
(23) Gu, Y.; Sun, W.; Wang, G.; Fang, N. Single particle orientation and rotation tracking discloses distinctive rotational dynamics of drug delivery vectors on live cell membranes. *J. Am. Chem. Soc.* **2011**, *133* (15), 5720−5723.
(24) Chakkarapani, S. K.; Sun, Y.; Lee, S.; Fang, N.; Kang, S. H. Three-dimensional orientation of anisotropic plasmonic aggregates at intracellular nuclear indentation sites by integrated light sheet super-resolution microscopy. *ACS Nano* **2018**, *12* (5), 4156−4163.
(25) Xiao, L.; Qiao, Y.; He, Y.; Yeung, E. S. Imaging translational and rotational diffusion of single anisotropic nanoparticles with planar illumination microscopy. *J. Am. Chem. Soc.* **2011**, *133* (27), 10638−10645.
(26) Li, T.; Li, Q.; Xu, Y.; Chen, X.-J.; Dai, Q.-F.; Liu, H.; Lan, S.; Tie, S.; Wu, L.-J. Three-dimensional orientation sensors by defocused imaging of gold nanorods through an ordinary wide-field microscope. *ACS Nano* **2012**, *6* (2), 1268−1277.
(27) Kim, G. W.; Lee, S. Y.; Ha, J. W. Three-dimensional defocused orientation sensing of single bimetallic core−shell gold nanorods as multifunctional optical probes. *Analyst* **2017**, *142* (6), 899−903.
(28) Ha, J. W. Characteristic image patterns of single anisotropic plasmonic nanoparticles embedded in a gel matrix. *Nanoscale* **2015**, *7* (31), 13159−13163.
(29) Stender, A. S.; Marchuk, K.; Liu, C.; Sander, S.; Meyer, M. W.; Smith, E. A.; Neupane, B.; Wang, G.; Li, J.; Cheng, J.-X.; Huang, B.; Fang, N. Single cell optical imaging and spectroscopy. *Chem. Rev.* **2013**, *113* (4), 2469−2527.
(30) Kim, G. W.; Yoon, S.; Lee, J.; Lee, J. H.; Ha, J. W. High-throughput characterization and in situ control of three-dimensional orientations of single gold nanorods coated with spherical mesoporous silica shell. *J. Phys. Chem. C* **2020**, *124* (26), 14279−14286.
(31) Kim, G. W.; Yoon, S.; Lee, J. H.; Ha, J. W. High-throughput in-focus differential interference contrast imaging of three-dimensional orientations of single gold nanorods coated with a mesoporous silica shell. *RSC Adv.* **2020**, *10* (50), 29868−29872.
(32) Yoon, S.; Lee, B.; Kim, C.; Lee, J. H. Controlled heterogeneous nucleation for synthesis of uniform mesoporous silica-coated gold nanorods with tailorable rotational diffusion and 1 nm-scale size tunability. *Cryst. Growth Des.* **2018**, *18* (8), 4731−4736.
(33) Gorelikov, I.; Matsuura, N. Single-step coating of mesoporous silica on cetyltrimethyl ammonium bromide-capped nanoparticles. *Nano Lett.* **2008**, *8* (1), 369−373.
(34) Yoon, S.; Lee, B.; Yun, J.; Han, J. G.; Lee, J.-S.; Lee, J. H. Systematic study of interdependent relationship on gold nanorod synthesis assisted by electron microscopy image analysis. *Nanoscale* **2017**, *9* (21), 7114−7123.
(35) Patra, D.; Gregor, I.; Enderlein, J.; Sauer, M. Defocused imaging of quantum-dot angular distribution of radiation. *Appl. Phys. Lett.* **2005**, *87* (10), No. 101103, DOI: 10.1063/1.2037194.
(36) Böhmer, M.; Enderlein, J. Orientation imaging of single molecules by wide-field epifluorescence microscopy. *J. Opt. Soc. Am. B* **2003**, *20* (3), 554−559.
(37) Lee, J.; Ha, J. W. Defocused dark-field orientation imaging of single gold microrods on synthetic membranes. *Phys. Chem. Chem. Phys.* **2017**, *19* (36), 24453−24457.
(38) Ha, J. W.; Marchuk, K.; Fang, N. Focused orientation and position imaging (FOPI) of single anisotropic plasmonic nanoparticles by total internal reflection scattering microscopy. *Nano Lett.* **2012**, *12* (8), 4282−4288.
(39) Chen, C.; Zhuang, X. Epsin 1 is a cargo-specific adaptor for the clathrin-mediated endocytosis of the influenza virus. *Proc. Natl. Acad. Sci. U.S.A.* **2008**, *105* (33), 11790−11795.
(40) Mettlen, M.; Pucadyil, T.; Ramachandran, R.; Schmid, S. L. Dissecting dynamin's role in clathrin-mediated endocytosis. *Biochem. Soc. Trans.* **2009**, *37*, 1022−1026.
(41) Ayscough, K. R. Defining protein modules for endocytosis. *Cell* **2005**, *123* (2), 188−190.
(42) Bashkirov, P. V.; Akimov, S. A.; Evseev, A. I.; Schmid, S. L.; Zimmerberg, J.; Frolov, V. A. GTPase cycle of dynamin is coupled to membrane squeeze and release, leading to spontaneous fission. *Cell* **2008**, *135* (7), 1276−1286.
(43) Cheng, X.; Chen, K.; Dong, B.; Yang, M.; Filbrun, S. L.; Myoung, Y.; Huang, T.-X.; Gu, Y.; Wang, G.; Fang, N. Dynamin-dependent vesicle twist at the final stage of clathrin-mediated endocytosis. *Nat. Cell Biol.* **2021**, *23* (8), 859−869.
(44) Sweitzer, S. M.; Hinshaw, J. E. Dynamin undergoes a GTP-dependent conformational change causing vesiculation. *Cell* **1998**, *93* (6), 1021−1029.
(45) Chappie, J. S.; Mears, J. A.; Fang, S.; Leonard, M.; Schmid, S. L.; Milligan, R. A.; Hinshaw, J. E.; Dyda, F. A Pseudoatomic model of the dynamin polymer identifies a hydrolysis-dependent powerstroke. *Cell* **2011**, *147* (1), 209−222.
(46) Colom, A.; Redondo-Morata, L.; Chiaruttini, N.; Roux, A.; Scheuring, S. Dynamic remodeling of the dynamin helix during membrane constriction. *Proc. Natl. Acad. Sci. U.S.A.* **2017**, *114* (21), 5449−5454.
(47) Chen, K.; Gu, Y.; Sun, W.; Bin, D.; Wang, G.; Fan, X.; Xia, T.; Fang, N. Characteristic rotational behaviors of rod-shaped cargo revealed by automated five-dimensional single particle tracking. *Nat. Commun.* **2017**, *8* (1), No. 887.
(48) Mears, J. A.; Ray, P.; Hinshaw, J. E. A Corkscrew model for dynamin constriction. *Structure* **2007**, *15* (10), 1190−1202.
(49) Gao, S.; von der Malsburg, A.; Paeschke, S.; Behlke, J.; Haller, O.; Kochs, G.; Daumke, O. Structural basis of oligomerization in the stalk region of dynamin-like MxA. *Nature* **2010**, *465* (7297), 502−506.

https://doi.org/10.1021/jacsau.3c00594
JACS Au 2023, 3, 3436−3445